Nanoscale Advances

ROYAL SOCIETY OF CHEMISTRY

PAPER

View Article Online
View Journal | View Issue

Cite this: *Nanoscale Adv.*, 2020, **2**, 512

NiS_2 nanoparticles anchored on open carbon nanohelmets as an advanced anode for lithium-ion batteries†

D. D. Yang, M. Zhao, R. D. Zhang, Y. Zhang, C. C. Yang * and Q. Jiang

Low intrinsic conductivity and large volume expansion seriously restrict the efficient lithium storage performance of metal sulfides. Here, we fabricate a hybrid material of NiS_2 nanoparticles/carbon nanohelmets (NiS_2/CNHs) to address the above issues. As an anode material in lithium-ion batteries, NiS_2/CNHs exhibit excellent cycling stability (490 mA h g^{-1} after 3000 cycles at 5 A g^{-1}) and rate properties (412 mA h g^{-1} at 10 A g^{-1}), outperforming other NiS_x-based anode materials. These remarkable performances originate from the three-dimensional helmet-like integrated architecture of NiS_2/CNHs, which reduces the electrode resistance due to the tight combination between NiS_2 and CNHs, provides efficient diffusion paths for the electrolyte and Li^+ owing to the amorphous nanoporous carbon structure, and significantly mitigates the aggregation and buffers the large volumetric expansion of NiS_2 nanoparticles upon long-term cycling thanks to the open three-dimensional architecture and well-dispersed NiS_2 nanoparticles on it.

Received 18th October 2019
Accepted 13th December 2019

DOI: 10.1039/c9na00661c

rsc.li/nanoscale-advances

Introduction

Lithium-ion batteries (LIBs), as efficient energy storage devices, have been widely used in consumer electronics and electric vehicles due to their high energy density, light weight, long life span and environmental benignity.[1–5] In this context, developing advanced electrode materials with excellent electrochemical performance is of great importance to cater to the growing requirements of large-scale practical applications.[6–9] To date, a large number of LIB anode materials, such as carbonaceous materials,[10,11] alloys (NiSn, CuZn, SiCu, *etc.*),[12–14] metal oxides (Fe_2O_3, SnO_2, CoO_2, TiO_2, *etc.*),[15–18] and metal nitrides and sulfides (Ni_3N, Fe_3N, MoS_2, CoS_2, SnS_2, *etc.*),[19–23] have been extensively studied. Among the various candidates, transition metal sulfides (TMSs) have enormous potential due to their higher electronic conductivity, much better cycling performance and higher theoretical capacity than those of their metal oxide counterparts.[24] In particular, NiS_2 attracted many researchers' attention owing to its high theoretical capacity (870 mA h g^{-1}). Nevertheless, the inherent relatively low conductivity and huge volume change during the charge/discharge process restrict the electrochemical performance of NiS_2 in LIBs.[25,26]

To tackle the aforementioned issues, many effective strategies have been proposed to construct advanced NiS_2 nanostructures and their hybrid materials. In this regard, the hybridization of NiS_2 with carbon-based materials is an effective approach to improve the electrochemical properties.[25–27] For example, Chen *et al.* reported that a composite of NiS_2/graphene delivered a reversible capacity as high as 810 mA h g^{-1} at a current density of 500 mA g^{-1} after 1000 cycles.[26] Lou *et al.* synthesized a NiS_2@C hybrid material, which exhibits excellent rate performance and a reversible capacity of 577 mA h g^{-1} at 2000 mA g^{-1}.[27] However, achieving both superior cycle stability and rate performance is highly desirable. Recently, Yang *et al.* synthesized a hybrid structure by anchoring NiO nanoparticles on open helmet-like carbon skeletons (NiO/CNHs), which shows both excellent long-term cycling performance (424 mA h g^{-1} after 1500 cycles at 7.5C) and rate performance (450 mA h g^{-1} at 15C).[28] Such a unique carbon nanoarchitecture is expected to also be applicable for NiS_2 nanoparticles.

Herein, a hybrid material of NiS_2 nanoparticles/carbon nanohelmets (NiS_2/CNHs) was fabricated through the sulfurization of NiO/CNHs. The NiS_2/CNH hybrid material has the following advantages: (1) the tight combination between NiS_2 nanoparticles and CNHs can greatly improve the overall conductivity of the hybrid material; (2) the CNH structure can be used as a matrix for dispersing NiS_2 nanoparticles uniformly, avoiding their self-aggregation and thus increasing the active sites for Li^+ insertion/extraction; (3) the porous CNHs can provide efficient electrolyte pathways and accelerate carrier transfer; (4) the open CNH skeleton can effectively alleviate the internal stress caused by the large volume change of NiS_2

Key Laboratory of Automobile Materials (Jilin University), Ministry of Education, School of Materials Science and Engineering, Jilin University, Changchun 130022, China. E-mail: ccyang@jlu.edu.cn; Fax: +86-431-85095876; Tel: +86-431-85095371

† Electronic supplementary information (ESI) available. See DOI: 10.1039/c9na00661c

nanoparticles during the charge/discharge process. As expected, the NiS_2/CNH hybrid material exhibits superior rate performance (412 mA h g^{-1} at 10 A g^{-1}) and excellent long-term cycling stability (490 mA h g^{-1} after 3000 cycles at 5 A g^{-1}) as an ideal anode material in LIBs.

Results and discussion

Materials synthesis and characterization

The fabrication procedure of the NiS_2/CNH hybrid material is schematically illustrated in Fig. 1. The field-emission scanning electron microscope (FESEM) images of the corresponding products, including SiO_2 spheres, resorcinol and formaldehyde resin/SiO_2 spheres (RF/SiO_2), $Ni(OH)_2$/RF/SiO_2, NiO/C/SiO_2 and NiO/CNHs, are shown in Fig. S1–S5.† Firstly, RF resin shells were formed on the surface of the SiO_2 template spheres with a polymerization process. Then, $Ni(OH)_2$ was grown on the surface of RF/SiO_2 *via* a hydrothermal reaction followed by a pyrolysis treatment under nitrogen protection to obtain NiO/C/SiO_2. Afterwards, NiO/CNH hybrids were obtained through a template removal method in NaOH solution. Here, the formation mechanism of the CNHs can be described as follows. During the carbonization process, some gaseous products (CO_2, CO, H_2O, CH_4, H_2, *etc.*) were generated from the pyrolysis of RF, which escaped from the system once their pressure became high enough. The plasticity of the carbon shell was weakened due to the pressure impact and the large number of pores created by the release of gaseous products. During the etching process of SiO_2, the Si–O–C interconnections were destroyed, resulting in a decrease of the interfacial tension force. As a result, the shrinkage of carbon shells occurred under the influence of constrictive forces from NiO. With the continuous increase of the shrinkage degree, it was difficult for the highly porous hollow carbon skeleton to withstand the shrinkage force, and it eventually fractured to form the CNH structure.[28] In addition, the intense agitation forces during the etching process also play an important role in accelerating the fracture of the hollow structure. Finally, NiO/CNHs were sulfurized with sublimed sulfur in a quartz tube reactor to obtain the NiS_2/CNH composite. It is known that Ni-based oxides and sulfides undergo conversion in LIBs. In general, TMSs exhibit higher electronic conductivity than their metal oxide counterparts.[24] Moreover, the metal–sulfur bonds in TMSs are relatively weaker than the metal–oxygen bonds in transition metal oxides (TMOs) due to the lower electronegativity of S compared with O, which is favorable for the conversion reaction for TMSs during the charge/discharge process in LIBs.[29,30] Note that the sulfurization process of NiO/CNHs was conducted under conditions of nitrogen protection, high sulfur content and high temperature. The corresponding conversion reaction from NiO to NiS_2 can be expressed using:

$$2NiO\ (s) + 5S\ (g) \rightarrow 2NiS_2\ (s) + SO_2\ (g). \quad (1)$$

Such an approach has been reported in previous studies.[31,32] For example, Wu *et al.* synthesized a hybrid of NiS_2 nanosheets grown on a graphite substrate *via* the sulfidation of NiO nanosheets with S vapor at 350 °C under argon protection.[31] Li *et al.* reported that NiO hollow spheres were sulfurized to NiS_2 by using sulfur powder at 350 °C under an argon atmosphere.[32] For comparison, a sample of pristine NiS_2 was also fabricated by sulfurization of NiO without the CNH skeleton. All materials synthesis details are provided in the Experimental section (see the ESI† for details).

Fig. 2a compares the X-ray diffraction (XRD) patterns of NiS_2/CNHs and pristine NiS_2. For each sample, the characteristic peaks at 27.1°, 31.4°, 35.3°, 38.8°, 45.1° and 53.4° can be indexed to the (111), (200), (210), (211), (220) and (311) planes, respectively, of the cubic NiS_2 phase with the $Pa\bar{3}$ space group (JCPDF no. 89-7142). Moreover, for NiS_2/CNHs, the broad peak between 20° and 30° is assigned to the characteristic structure of amorphous carbon.[28,33] Fig. 2b shows the Raman spectrum of NiS_2/CNHs, in which two typical peaks at 1360 and 1586 cm^{-1} are assigned to the D band and G band of carbon, respectively.[34] The calculated value of I_D/I_G is 1.00, demonstrating the abundance of topological defects and disorders in CNHs, which are beneficial for lithium storage.[35] The nitrogen adsorption/desorption isotherm (see Fig. 2c) of NiS_2/CNHs exhibits a type-IV behavior with a representative hysteresis loop in the relative pressure range of 0.45–1 that can be linked to a large amount of mesopores in NiS_2/CNHs.[36,37] From the inset curve of Fig. 2c, the sizes of most pores are concentrated within 2–10 nm, while other pores exhibit a wide size distribution between 10 and 100 nm. Moreover, the NiS_2/CNHs exhibit a relatively large specific surface area of 96.62 m^2 g^{-1}. The large specific surface area and the high porosity result in a large electrode–electrolyte contact area and fast Li^+ transport, which are beneficial for high discharge capacity and excellent rate

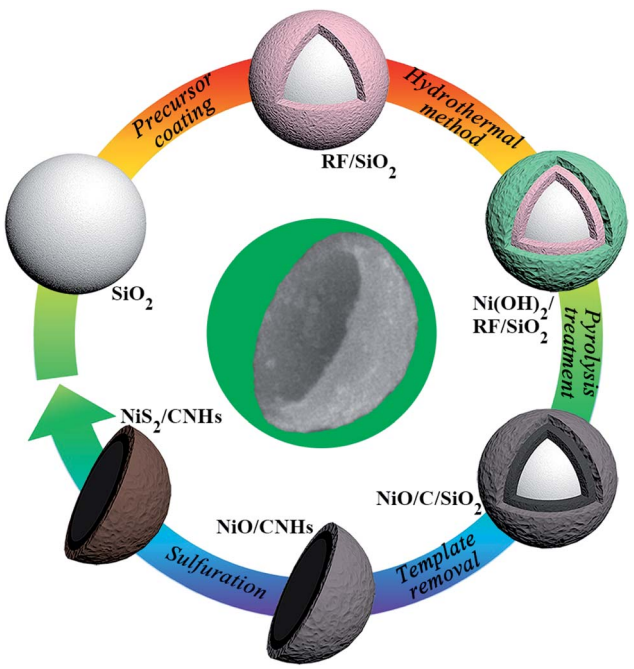

Fig. 1 Schematic illustration of the synthesis procedure of NiS_2/CNHs.

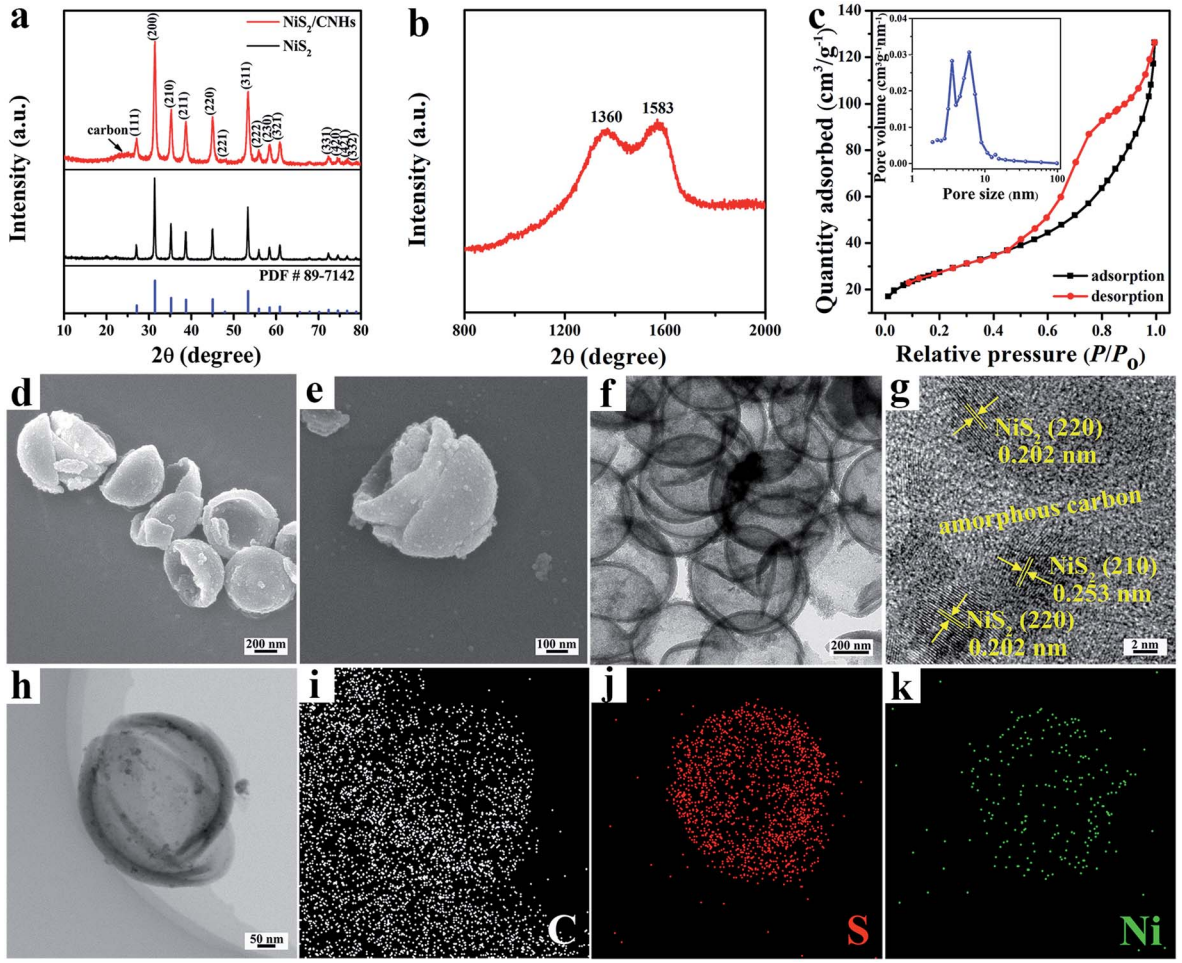

Fig. 2 Structural and morphological characterization. (a) XRD patterns of pristine NiS_2 and NiS_2/CNHs. (b) Raman spectrum of NiS_2/CNHs. (c) N_2 adsorption/desorption isotherms and pore size distribution (the inset) of NiS_2/CNHs. (d and e) FESEM images of NiS_2/CNHs at different magnifications. (f) TEM image of NiS_2/CNHs. (g) HRTEM image of NiS_2/CNHs. (h) TEM image of NiS_2/CNHs and corresponding elemental maps for (i) C, (j) S and (k) Ni elements.

performance.[38,39] Fig. 2d and e present the FESEM images of NiS_2/CNHs, where hollow CNHs are formed with heights of 200–300 nm and diameters of 400–600 nm. It is obvious that the NiS_2 nanoparticles are uniformly dispersed on CNHs without the accumulation of many nanoparticles. In contrast, the NiS_2 nanoparticles without CNHs as a carrier aggregated into a bulk one (see Fig. S6†), which demonstrates that CNHs can effectively inhibit the agglomeration of NiS_2 nanoparticles. Fig. 2f shows a transmission electron microscopy (TEM) image of NiS_2/CNHs, further confirming the uniform dispersion of NiS_2 nanoparticles on the CNH skeleton. Such an open structure can greatly alleviate the huge volume change of NiS_2 during the charge/discharge process and thus enhance the cycle stability of NiS_2/CNHs. It should be mentioned that the inner carbon layer in the open NiS_2/CNHs shows structural advantages for lithium storage by (i) providing a large number of active sites for Li^+ insertion/extraction, which is beneficial for the enhancement of the specific capacity; (ii) providing efficient diffusion paths for the electrolyte and Li^+; and (iii) significantly reducing the internal resistance contributed by the contact between NiS_2 and the inner carbon layer. Fig. 2g presents a high-resolution TEM image of NiS_2/CNHs, in which the interplanar spacings of 0.202 nm and 0.253 nm correspond to the (220) and (210) planes of NiS_2, respectively. From the figure, NiS_2 nanoparticles are all surrounded by amorphous carbon, indicating the excellent contact between them. Fig. S7† exhibits a TEM image and particle size distribution (the inset) of NiS_2/CNHs, where the mean size of NiS_2 nanoparticles is 8.10 nm. Such small nanoparticles provide abundant active sites for Li^+ insertion/extraction, increasing the reversible capacity of the NiS_2/CNHs. Moreover, the TEM and elemental mapping images display homogeneous distributions of S and Ni along the CNH skeleton (see Fig. 2h–k). To further determine the content of active material in NiS_2/CNHs, a thermogravimetric analysis (TGA) test was carried out. As exhibited in Fig. S8,† the volatilization of water contained in the NiS_2/CNHs occurred below the temperature of 250 °C. The mass loss above 250 °C was ascribed to the oxidation of NiS_2 and carbon. Thus, the content of NiS_2 in the NiS_2/CNHs is calculated to be 83.8%, based on the equation in Fig. S8.†

The chemical composition and surface electronic state of C, S and Ni elements in NiS_2/CNHs were further investigated by X-ray photoelectron spectroscopy (XPS). The survey spectrum reveals that the primary elements in NiS_2/CNHs are C, S, Ni and O (see Fig. 3a). As presented in Fig. 3b, the high resolution XPS spectrum of C 1s has three obvious peaks, which correspond to the strong C–C bond (284.8 eV), C–O bond (285.5 eV) and weaker C=O bond (288.8 eV), respectively.[40,41] Five fitted peaks exist in the S 2p spectrum (see Fig. 3c) where the two strong peaks at 162.6 and 163.85 eV are attributed to $2p_{3/2}$ and $2p_{1/2}$ of the S element in the NiS_2, indicating the presence of S–S bonds in the NiS_2/CNHs. In addition, a pair of peaks around 163.55 eV and 164.7 eV are assigned to the residual S (α-S_8) in NiS_2/CNHs, which may be retained during the sulfurization process.[42,43] The peak located at 169.0 eV is ascribed to the S–O covalent bond due to the surface oxidation of the NiS_2/CNHs.[41,44] Note that elemental sulfur is not detected in the XRD pattern, indicating its trace amount.[45] Fig. 3d shows the high resolution XPS spectrum of Ni 2p, which exhibits three pairs of peaks. The peaks situated at 854.2 and 871.75 eV are attributed to $2p_{3/2}$ and $2p_{1/2}$ of Ni^{2+}, while the peaks located at 856.05 and 875.1 eV are assigned to $2p_{3/2}$ and $2p_{1/2}$ of Ni^{3+}. In addition, the two other peaks at 861.35 and 879.5 eV are ascribed to the satellite peaks of Ni $2p_{3/2}$ and Ni $2p_{1/2}$, respectively.[25,46]

Electrochemical performance

Fig. 4a presents the cyclic voltammetry (CV) curves of the NiS_2/CNH electrode for the initial five cycles within a voltage window of 0.01–3.0 V (*vs.* Li^+/Li) at a constant scan rate of 0.1 mV s^{-1}. During the first cathodic scan process, two strong peaks located at 1.50 V and 1.18 V are attributed to the intercalation of Li^+ into the NiS_2 lattice to form Li_xNiS_2 and the following conversion reaction process from Li_xNiS_2 to Ni and Li_2S, respectively.[26,27] It is noteworthy that the pronounced cathodic peak at 0.69 V, which disappears in the subsequent cycles, corresponds to the formation of an irreversible solid–electrolyte interface (SEI) layer.[26,27] Furthermore, a weak peak at 1.68 V can be attributed to the lithiation reaction of a trace amount of residual sulfur in the NiS_2/CNHs.[47] For the reverse anodic scan process, the part of lithium stored at the defects will be removed first, which generates a peak at about 1.16 V.[26] Two remarkable peaks at 2.01 V and 2.22 V are associated with the formation of Li_xNiS_2 and NiS_2, respectively.[25,27,48] The peak at 2.36 V, gradually weakened in the subsequent cycles, is ascribed to the conversion of Li_2S to S. Moreover, in the following cathodic sweep, the peak at 1.91 V and the extremely slight peaks nearby are attributed to the multi-step lithiation of S.[26] From the second cycle onward, the cathodic peaks at 1.50 V and 1.18 V slightly shift to 1.58 V and 1.27 V, respectively. Note that the CV profiles show little difference with increasing cycles from the third cycle, indicating the excellent cycling stability of the NiS_2/CNH electrode. According to previous studies,[26,27,48] the corresponding lithium storage conversion reactions can be expressed using the following equations:

$$NiS_2 + xLi^+ + xe^- \leftrightarrow Li_xNiS_2 \quad (2)$$

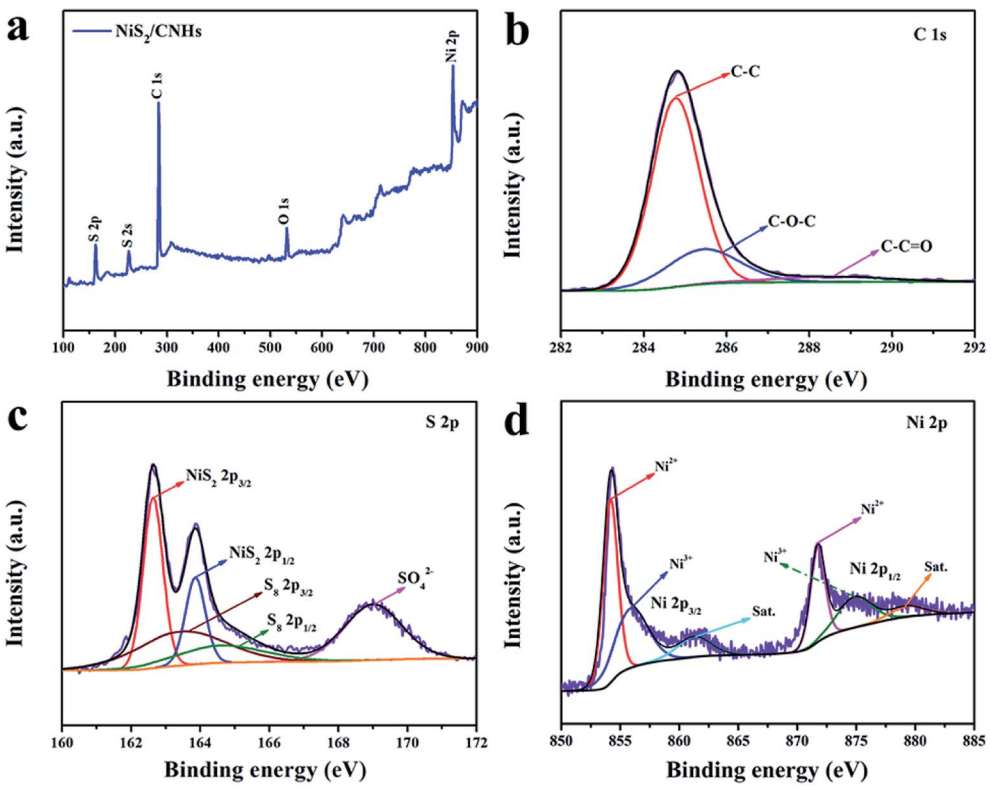

Fig. 3 XPS analysis. (a) The survey XPS spectrum of NiS_2/CNHs. (b–d) High-resolution XPS spectra of C 1s, S 2p and Ni 2p, respectively, of NiS_2/CNHs.

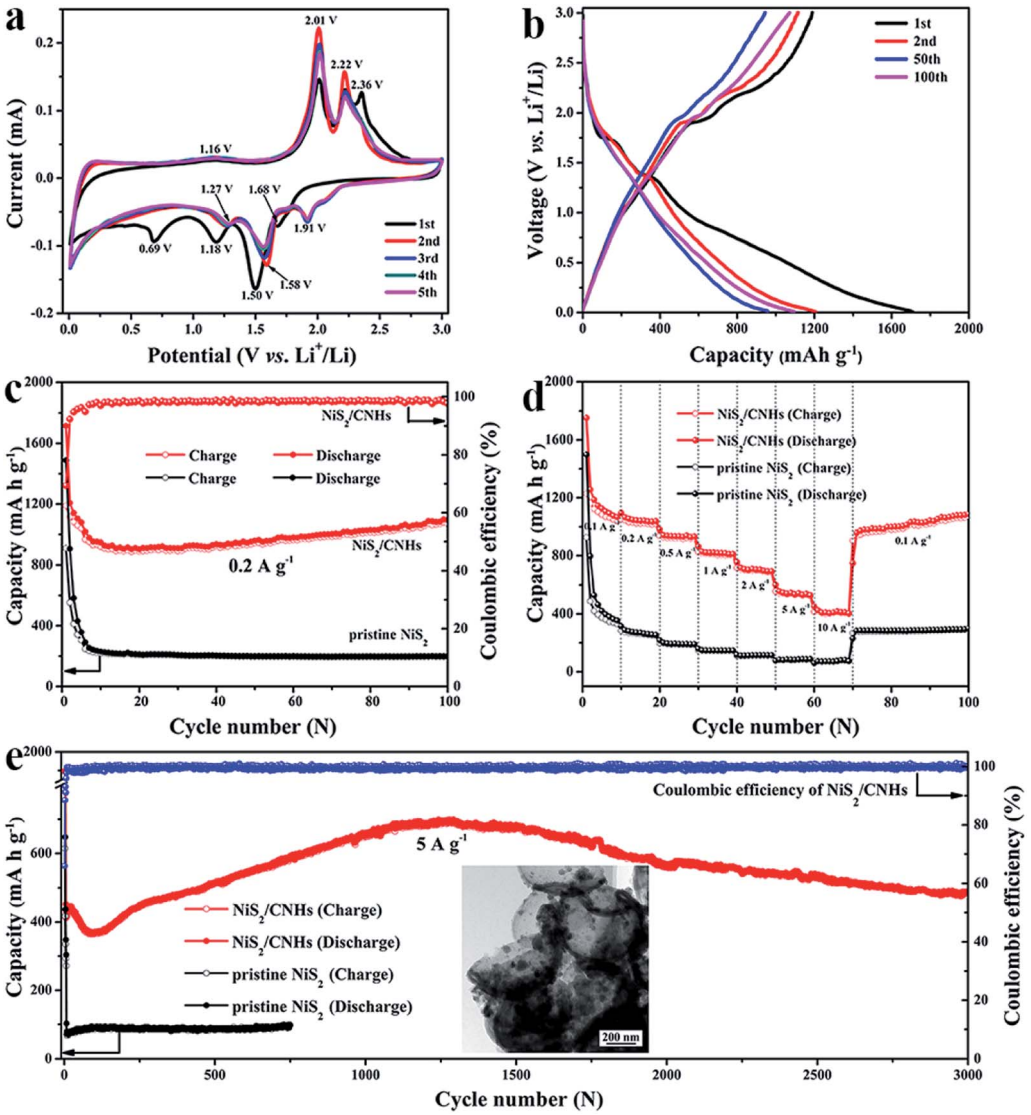

Fig. 4 Electrochemical performances of the NiS_2/CNH electrode in LIBs. (a) CV curves of the NiS_2/CNH electrode at a scan rate of 0.1 mV s^{-1}. (b) Galvanostatic discharge/charge curves of the NiS_2/CNH electrode at a current density of 0.2 A g^{-1}. (c) Cycling performance and coulombic efficiency of the pristine NiS_2 and NiS_2/CNH electrodes at a current density of 0.2 A g^{-1}. (d) Rate performance of the pristine NiS_2 and NiS_2/CNH electrodes at different current densities. (e) Long-term cycling performance and coulombic efficiency of the pristine NiS_2 and NiS_2/CNH electrodes at a current density of 5 A g^{-1} and the TEM image after 2000 cycles (the inset).

$$Li_xNiS_2 + (4 - x)Li^+ + (4 - x)e^- \leftrightarrow Ni + 2Li_2S. \quad (3)$$

The galvanostatic charge/discharge profiles of the NiS_2/CNH electrode for the 1st, 2nd, 50th and 100th cycles at a current density of 0.2 A g^{-1} are shown in Fig. 4b. The NiS_2/CNH electrode delivers high first-cycle discharge and charge capacities of 1714.5 and 1189.2 mA h g^{-1}, respectively, with an initial coulombic efficiency of 69.36%. The high irreversible capacity loss during the first cycle can be attributed to the formation of the SEI layer.[49–52] The inconspicuous voltage plateaus in Fig. 4b may be attributed to the complicated multi-step reactions of NiS_2, the pseudocapacitive behavior of nanosized-NiS_2 particles, and the partial effect from the sloping voltage curve of carbonaceous material.[53–57] Such a phenomenon has also been reported for various TMS anode materials in previous studies.[27,51,58] In this work, the NiS_2/CNH electrode material exhibits high specific capacity and excellent cycling stability and rate performance. In addition, most of the charge capacity is released below a voltage of 1.5 V, which is beneficial to improving the energy density of batteries.[59,60] Thus, the NiS_2/CNH hybrid has great potential for application in high-performance LIBs in the near future. Note that the active material is the NiS_2/CNH hybrid and all the capacities recorded in this work are calculated on the basis of the total mass of NiS_2/CNHs. The cycling performances of NiS_2/CNH and pristine NiS_2 electrodes at a current density of 0.2 A g^{-1} are shown in Fig. 4c. The NiS_2/CNH hybrid electrode exhibits an excellent cycling performance with a specific capacity of 1096 mA h g^{-1} after 100 cycles, which is much higher than that of the pristine NiS_2

electrode (only 199 mA h g^{-1}). Moreover, the coulombic efficiency of the NiS_2/CNH electrode is close to 100%, indicating its excellent reversibility during the Li^+ insertion/extraction process. The discharge capacity of the NiS_2/CNH electrode drops from 1714.5 mA h g^{-1} to 902.2 mA h g^{-1} in the first 20 cycles and then increases gradually to a value as high as 1096 mA h g^{-1} after 100 cycles. To the best of our knowledge, this phenomenon of capacity increase is common in metal oxide/sulfide composites and is normally ascribed to the improved charge transfer kinetics by the reversible reaction between metal nanoparticles and electrolytes and the gradual activation process during the cycling process.[51,61] However, it is apparent that the capacity retention for the pristine NiS_2 electrode is very poor and shows a monotonous decreasing trend. Fig. 4d compares the rate performance of the NiS_2/CNH and pristine NiS_2 electrodes. The excellent rate performance of NiS_2/CNHs is evidenced by the average specific capacities of 1112, 1045, 935, 819, 706, 541 and 412 mA h g^{-1} at current densities of 0.1, 0.2, 0.5, 1, 2, 5 and 10 A g^{-1}, respectively. Moreover, the reversible capacity of the NiS_2/CNH electrode rapidly recovers to 1087.1 mA h g^{-1} in the 30th cycle when the current density is changed back to 0.1 A g^{-1} and then maintains a continuous increase during further cycling, while the pristine NiS_2 electrode shows a much worse performance at each current density. The superior rate performance of NiS_2/CNHs is attributed to the low internal resistance, which has been demonstrated by the electrochemical impedance spectroscopy (EIS) measurement results shown in Fig. S9.† The NiS_2/CNH electrode displays a smaller intrinsic electrode/electrolyte resistance R_{el} (=1.9 Ω) and charge transfer resistance R_{ct} (=57 Ω) than the pristine NiS_2 electrode (2.5 Ω and 143 Ω, respectively). In addition, the large specific surface area and pore volume of NiS_2/CNHs provide efficient diffusion pathways for Li^+ and the electrolyte, which is also beneficial for achieving excellent rate performance. Furthermore, Fig. S10† displays the comparison of the rate performance between the NiS_2/CNH electrode in this work and previously reported NiS_x-based anode materials. It is obvious that NiS_2/CNHs show the best rate performance among them.

To evaluate the long-term cycling stability of the NiS_2/CNH electrode, it was galvanostatically discharged and charged at 0.1 A g^{-1} for the first five cycles and then at 5 A g^{-1} for 3000 cycles. The corresponding results are shown in Fig. 4e. The hybrid electrode suffers from capacity fluctuations during long-term cycling. After the first 100 cycles, the specific capacity of the hybrid electrode drops from 1790 mA h g^{-1} to 370 mA h g^{-1}, resulting from the formation of the SEI film and irreversible transformation from NiS_2 to metallic Ni nanoparticles.[28,62] Then, the specific capacity increases gradually to the maximum capacity (699.4 mA h g^{-1}) in the 1292nd cycle. Such a capacity increase can be attributed to the improved charge transfer kinetics during the gradual activation process and reversible reaction between Ni nanoparticles and electrolytes. This phenomenon has also been observed in other composites of TMOs/TMSs and carbon.[51,63,64] In addition, electrochemical impedance spectroscopy (EIS) of the NiS_2/CNH electrode after the 100th and 350th cycles was performed and the corresponding results are shown in Fig. S11.† It is found that the electrode/electrolyte resistance R_{el} (=3.2 Ω) and charge transfer resistance R_{ct} (=34.3 Ω) values in the 350th cycle are smaller than those in the 100th cycle (R_{el} = 3.7 Ω and R_{ct} = 44.7 Ω). Note that the impedance decreases gradually with the increasing cycles and the R_{ct} values after cycling are lower than that of the fresh cell (R_{ct} = 57 Ω). This phenomenon should be attributed to the *in situ* generated Ni from the incomplete conversion reactions which could enhance the electronic conductivity of the electrode.[28,64] As shown in Fig. S11,† there exist two semicircles in the high-frequency region, suggesting the formation of a new phase (Ni nanoparticles), which is also consistent with the above analysis results.[28,65] Finally, the specific capacity decreases gradually to 490 mA h g^{-1} after 3000 cycles. This may be ascribed to the falling off of some active materials caused by the volume expansion during the long-term continuous charge/discharge process.[50] In contrast, the specific capacity of the pristine NiS_2 electrode is only 97.6 mA h g^{-1} after 750 cycles. As exhibited in the inset TEM image in Fig. 4e, the NiS_2/CNH hybrid retains its original helmet-like skeleton after 2000 cycles, which indicates its excellent structural stability. Besides, Fig. S12† shows a FESEM image of the NiS_2/CNH electrode after 2000 cycles, further demonstrating the good integrity of the electrode material after long-term cycling.

As listed in Table S1,† the NiS_2/CNH electrode exhibits the best cycling stability and rate performance among currently reported NiS_x-based anode materials.[24–26,39,46,48,49,66–68] The excellent electrochemical performance of NiS_2/CNHs can be attributed to their characteristic structure with the following advantages: (1) well-dispersed NiS_2 nanoparticles on CNHs can effectively mitigate the aggregation and buffer the volumetric expansion of NiS_2 nanoparticles upon long-term cycling; (2) the tight combination between NiS_2 nanoparticles and CNHs can greatly improve the overall conductivity of the NiS_2/CNH electrode; and (3) the three-dimensional nanoporous carbon architecture can provide efficient diffusion paths for the electrolyte and Li^+ to fully come into contact with electrochemically active NiS_2 nanoparticles.

Conclusion

In summary, we have successfully fabricated a hybrid material of NiS_2/CNHs, which combines the advantages of the high conductivity and good stability of the carbon material and the high theoretical capacity of NiS_2. Benefiting from the above superior properties, when tested as an anode in LIBs, the NiS_2/CNH electrode exhibits superior rate performance (412 mA h g^{-1} at 10 A g^{-1}) and excellent cycling stability (490 mA h g^{-1} after 3000 cycles at 5 A g^{-1}), outperforming other NiS_x-based materials and making it a promising candidate as an anode material for highly reversible lithium storage.

Conflicts of interest

There are no conflicts to declare.

Acknowledgements

This project is financially supported by National Natural Science Foundation of China (No. 51671092 and 51631004), Project of Talent Development in Jilin Province, Program for JLU Science and Technology Innovative Research Team (No. 2017TD-09), and the Fundamental Research Funds for the Central Universities.

References

1 D. Larcher and J.-M. Tarascon, *Nat. Chem.*, 2015, **7**, 19–29.
2 Y.-M. Chiang, *Science*, 2010, **330**, 1485–1486.
3 B. Dunn, H. Kamath and J.-M. Tarascon, *Science*, 2011, **334**, 928–935.
4 X. Hu, J. Jia, G. Wang, J. Chen, H. Zhan and Z. Wen, *Adv. Energy Mater.*, 2018, **8**, 1801452.
5 X. Su, Q. Wu, J. Li, X. Xiao, A. Lott, W. Lu, B. W. Sheldon and J. Wu, *Adv. Energy Mater.*, 2014, **4**, 1300882.
6 Y. Zhao, L. P. Wang, M. T. Sougrati, Z. Feng, Y. Leconte, A. Fisher, M. Srinivasan and Z. Xu, *Adv. Energy Mater.*, 2017, **7**, 1601424.
7 X. Feng, M. Ouyang, X. Liu, L. Lu, Y. Xia and X. He, *Energy Storage Materials*, 2018, **10**, 246–267.
8 X. Hu, Y. Li, G. Zeng, J. Jia, H. Zhan and Z. Wen, *ACS Nano*, 2018, **12**, 1592–1602.
9 J. Xu, F. Lin, M. M. Doeff and W. Tong, *J. Mater. Chem. A*, 2017, **5**, 874–901.
10 L. Qie, W.-M. Chen, Z.-H. Wang, Q.-G. Shao, X. Li, L.-X. Yuan, X.-L. Hu, W.-X. Zhang and Y.-H. Huang, *Adv. Mater.*, 2012, **24**, 2047–2050.
11 X. Liu, D. Chao, Y. Li, J. Hao, X. Liu, J. Zhao, J. Lin, H. J. Fan and Z. X. Shen, *Nano Energy*, 2015, **17**, 43–51.
12 J. Hassoun, S. Panero, P. Simon, P. L. Taberna and B. Scrosati, *Adv. Mater.*, 2007, **19**, 1632–1635.
13 A. Varzi, L. Mattarozzi, S. Cattarin, P. Guerriero and S. Passerini, *Adv. Energy Mater.*, 2018, **8**, 1701706.
14 H. Song, H. X. Wang, Z. Lin, X. Jiang, L. Yu, J. Xu, Z. Yu, X. Zhang, Y. Liu, P. He, L. Pan, Y. Shi, H. Zhou and K. Chen, *Adv. Funct. Mater.*, 2016, **26**, 524–531.
15 B. Wang, J. S. Chen, H. B. Wu, Z. Wang and X. W. Lou, *J. Am. Chem. Soc.*, 2011, **133**, 17146–17148.
16 X. W. Lou, Y. Wang, C. Yuan, J. Y. Lee and L. A. Archer, *Adv. Mater.*, 2006, **18**, 2325–2329.
17 S. Zhu, J. Li, X. Deng, C. He, E. Liu, F. He, C. Shi and N. Zhao, *Adv. Funct. Mater.*, 2017, **27**, 1605017.
18 Z. Wang and X. W. Lou, *Adv. Mater.*, 2012, **24**, 4124.
19 C. Chen, X. Xie, B. Anasori, A. Sarycheva, T. Makaryan, M. Zhao, P. Urbankowski, L. Miao, J. Jiang and Y. Gogotsi, *Angew. Chem., Int. Ed.*, 2018, **57**, 1846–1850.
20 L. Yu, J. F. Yang and X. W. Lou, *Angew. Chem., Int. Ed.*, 2016, **55**, 1–5.
21 J. Seo, J. Jang, S. Park, C. Kim, B. Park and J. Cheon, *Adv. Mater.*, 2008, **20**, 4269–4273.
22 M.-S. Balogun, Y. Zeng, W. Qiu, Y. Luo, A. Onasanya, T. K. Olaniyi and Y. Tong, *J. Mater. Chem. A*, 2016, **4**, 9844–9849.
23 H. Huang, S. Gao, A.-M. Wu, K. Cheng, X.-N. Li, X.-X. Gao, J.-J. Zhao, X.-L. Dong and G.-Z. Cao, *Nano Energy*, 2017, **31**, 74–83.
24 Z. Gao, N. Song, Y. Zhang and X. Li, *Nano Lett.*, 2015, **15**, 8194–8203.
25 Y. Zhang, F. Lu, L. Pan, Y. Xu, Y. Yang, Y. Bando, D. Golberg, J. Yao and X. Wang, *J. Mater. Chem. A*, 2018, **6**, 11978–11984.
26 Q. Chen, W. Chen, J. Ye, Z. Wang and J. Y. Lee, *J. Power Sources*, 2015, **294**, 51–58.
27 P. Lou, Y. Tan, P. Lu, Z. Cui and X. Guo, *J. Mater. Chem. A*, 2016, **4**, 16849–16855.
28 C. C. Yang, W. T. Jing, C. Li and Q. Jiang, *J. Mater. Chem. A*, 2018, **6**, 3877–3883.
29 X. Hu, Y. Liu, J. Chen, J. Jia, H. Zhan and Z. Wen, *J. Mater. Chem. A*, 2019, **7**, 1138–1148.
30 Y. Xiao, S. H. Lee and Y.-K. Sun, *Adv. Energy Mater.*, 2017, **7**, 1601329.
31 X. Wu, B. Yang, Z. Li, L. Lei and X. Zhang, *RSC Adv.*, 2015, **5**, 32976–32982.
32 D. Li, X. Zhao, R. Yu, B. Wang, H. Wang and D. Wang, *Inorg. Chem. Front.*, 2018, **5**, 535–540.
33 C. C. Yang, D. M. Zhang, L. Du and Q. Jiang, *J. Mater. Chem. A*, 2018, **6**, 12663–12671.
34 R. Bi, C. Zeng, H. Huang, X. Wang and L. Zhang, *J. Mater. Chem. A*, 2018, **6**, 14077–14082.
35 H.-G. Wang, Y. Wang, Y. Li, Y. Wan and Q. Duan, *Carbon*, 2015, **82**, 116–123.
36 J. Li, D. Yan, X. Zhang, S. Hou, T. Lu, Y. Yao and L. Pan, *J. Mater. Chem. A*, 2017, **5**, 20428–20438.
37 W. T. Jing, Y. Zhang, Y. Gu, Y. F. Zhu, C. C. Yang and Q. Jiang, *Matter*, 2019, **1**, 720–733.
38 C. Li, M. Zhao, C. N. Sun, B. Jin, C. C. Yang and Q. Jiang, *J. Power Sources*, 2018, **397**, 162–169.
39 A. A. AbdelHamid, X. Yang, J. Yang, X. Chen and J. Y. Ying, *Nano Energy*, 2016, **26**, 425–437.
40 W. Zhao, S. Ci, X. Hu, J. Chen and Z. Wen, *Nanoscale*, 2019, **11**, 4688–4695.
41 T. Tian, L. Huang, L. Ai and J. Jiang, *J. Mater. Chem. A*, 2017, **5**, 20985–20992.
42 Q. Chen, S. Sun, T. Zhai, M. Yang, X. Zhao and H. Xia, *Adv. Energy Mater.*, 2018, **8**, 1800054.
43 Y. Lu, X. Li, J. Liang, L. Hu, Y. Zhu and Y. Qian, *Nanoscale*, 2016, **8**, 17616–17622.
44 K. Liang, K. Marcus, S. Zhang, L. Zhou, Y. Li, S. T. D. Oliveira, N. Orlovskaya, Y.-H. Sohn and Y. Yang, *Adv. Energy Mater.*, 2017, **7**, 1701309.
45 G. Zhao, Y. Zhang, L. Yang, Y. Jiang, Y. Zhang, W. Hong, Y. Tian, H. Zhao, J. Hu, L. Zhou, H. Hou, X. Ji and L. Mai, *Adv. Funct. Mater.*, 2018, **28**, 1803690.
46 Y. Lin, Z. Qiu, D. Li, S. Ullah, Y. Hai, H. Xin, W. Liao, B. Yang, H. Fan, J. Xu and C. Zhu, *Energy Storage Materials*, 2018, **11**, 67–74.
47 J. Ruan, T. Yuan, Y. Pang, S. Luo, C. Peng, J. Yang and S. Zheng, *Carbon*, 2018, **126**, 9–16.
48 W. Pi, T. Mei, J. Li, J. Wang, J. Li and X. Wang, *Chem. Eng. J.*, 2018, **335**, 275–281.

49 J. Zhu, Y. Li, S. Kang, X.-L. Wei and P. K. Shen, *J. Mater. Chem. A*, 2014, **2**, 3142–3147.
50 P. Fan, H. Liu, L. Liao, J. Fu, Z. Wang, G. Lv, L. Mei, H. Hao, J. Xing and J. Dong, *RSC Adv.*, 2017, **7**, 49739–49744.
51 R. Wu, D. Wang, X. Rui, B. Liu, K. Zhou, A. W. K. Law, Q. Yan, J. Wei and Z. Chen, *Adv. Mater.*, 2015, **27**, 3038–3044.
52 H. Li, X. Wang, Z. Zhao, Z. Tian, D. Zhang and Y. Wu, *ChemElectroChem*, 2019, **6**, 404–412.
53 Y. F. Yuan, L. W. Ye, D. Zhang, F. Chen, M. Zhu, L. N. Wang, S. M. Yin, G. S. Cai and S. Y. Guo, *Electrochim. Acta*, 2019, **299**, 289–297.
54 H.-S. Kim, J. B. Cook, S. H. Tolbert and B. Dunn, *J. Electrochem. Soc.*, 2015, **162**, 5083–5090.
55 V. Augustyn, P. Simonbc and B. Dunn, *Energy Environ. Sci.*, 2014, **7**, 1597–1614.
56 Y. Chen, X. Li, K. Park, J. Song, J. Hong, L. Zhou, Y.-W. Mai, H. Huang and J. B. Goodenough, *J. Am. Chem. Soc.*, 2013, **135**, 16280–16283.
57 Q. Pan, J. Xie, S. Liu, G. Cao, T. Zhu and X. Zhao, *RSC Adv.*, 2013, **3**, 3899–3906.
58 H. Jiang, D. Ren, H. Wang, Y. Hu, S. Guo, H. Yuan, P. Hu, L. Zhang and C. Li, *Adv. Mater.*, 2015, **27**, 3687–3695.
59 C. Wu, P. Kopold, P. A. van Aken, J. Maier and Y. Yu, *Adv. Mater.*, 2017, **29**, 1604015.
60 L. Xiao, Y. Cao, W. A. Henderson, M. L. Sushko, Y. Shao, J. Xiao, W. Wang, M. H. Engelhard, Z. Nie and J. Liu, *Nano Energy*, 2016, **19**, 279–288.
61 Y. Du, Z. Yin, J. Zhu, X. Huang, X.-J. Wu, Z. Zeng, Q. Yan and H. Zhang, *Nat. Commun.*, 2012, **3**, 1177.
62 C. Peng, B. Chen, Y. Qin, S. Yang, C. Li, Y. Zuo, S. Liu and J. Yang, *ACS Nano*, 2012, **6**, 1074–1081.
63 H. Li, Y. Su, W. Sun and Y. Wang, *Adv. Funct. Mater.*, 2016, **26**, 8345–8353.
64 J. Luo, J. Liu, Z. Zeng, C. F. Ng, L. Ma, H. Zhang, J. Lin, Z. Shen and H. J. Fan, *Nano Lett.*, 2013, **13**, 6136–6143.
65 S. Venkatachalam, H. Zhu, C. Masarapu, K. Hung, Z. Liu, K. Suenaga and B. Wei, *ACS Nano*, 2009, **3**, 2177–2184.
66 X. Wang, X. Liu, G. Wang, Y. Zhou and H. Wang, *J. Power Sources*, 2017, **342**, 105–115.
67 L. Zhang, Y. Huang, Y. Zhang, H. Gu, W. Fan and T. Liu, *Adv. Mater. Interfaces*, 2016, **3**, 1500467.
68 X. Wu, S. Li, Y. Xu, B. Wang, J. Liu and M. Yu, *Chem. Eng. J.*, 2019, **356**, 245–254.